Journal of Theoretical and Applied Mechanics, Sofia, Vol.54 (2024) pp. 375-390
SPECIAL ISSUE

GREEN'S FUNCTIONS FOR THE VISCOELASTIC HALFSPACE: A CONVOLUTIONAL NEURAL NETWORK APPROACH

GEORGE D. MANOLIS[1], GEORGIOS I. DADOULIS[1],
PETIA S. DINEVA[2*], TSVIATKO V. RANGELOV[3]

[1]*Laboratory of Experimental Strength of Materials and Structures, Department of Civil Engineering, Aristotle University, Thessaloniki, GR-54124, Greece*
[2]*Institute of Mechanics, Bulgarian Academy of Sciences, Sofia 1113, Bulgaria*
[3]*Institute of Mathematics and Informatics, Bulgarian Academy of Sciences, Sofia 1113, Bulgaria*

[Received: 30 September 2024. Accepted: 14 December 2024]

doi: https://doi.org/10.55787/jtams.24.54.4.375

ABSTRACT: An identification problem in elastodynamics is addressed through the use of machine learning (ML) to recognize the presence of a free surface in a 3D viscoelastic continuum by measuring the dynamic response (displacements) at a receiver node due to an impulse at a source node. Specifically, a convolutional neural network (CNN) is constructed based on numerical solutions in the form of spectrograms, which are furnished through an implementation of the fundamental solutions of elastodynamics for both the full- and the half-spaces, while both frequency and time domains are considered. Following training of the CNN and its subsequent validation, data streams are evaluated and the results are given in the form 'confusion' matrices, which quantify the probability that a given displacement signal moves unimpeded or is being scattered. This in turn indicates the presence or absence of a free surface in the continuum. Furthermore, it is possible to re-train the CNN to estimate of the depth of the source point from the free surface, if such a surface exists. Finally, applications of this work are in areas ranging from geophysics to material science.

KEY WORDS: Green's functions; Machine learning; Elastodynamics; Wave propagation.

1 INTRODUCTION

Motivation. The original motivation for this work comes from geophysics, where from the processing of recorded ground motions at a receiver point on the surface it is possible to deduce various characteristics of the earthquake, such as depth of source, epicentral distance and magnitude [1,2], see Fig. 1. Similar problems emerge

*Corresponding author e-mail: petia@imbm.bas.bg

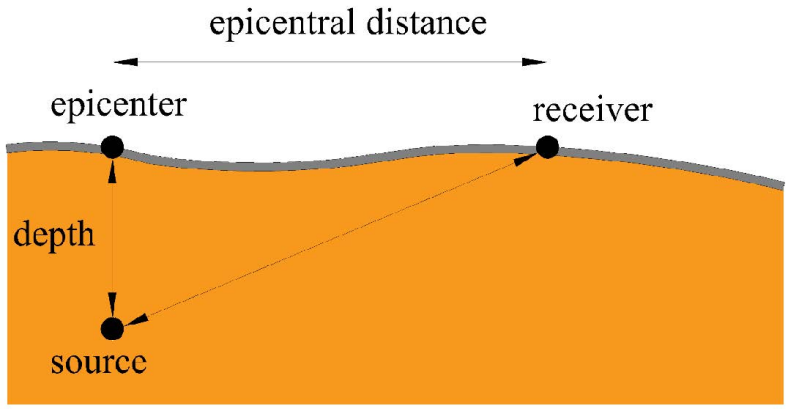

(a)

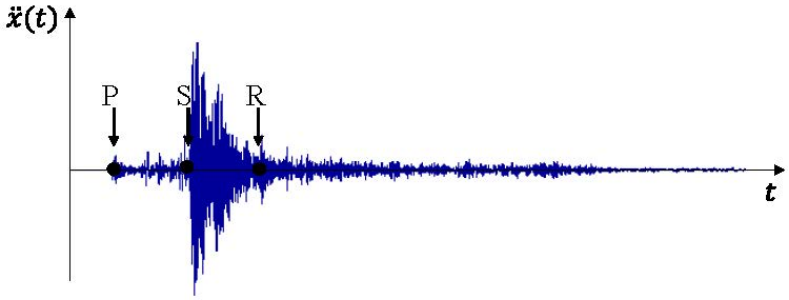

(b)

Fig. 1. (a) Generation of earthquakes in the lithosphere; (b) typical time recordings of seismic events at surface receivers indicating the arrival of Pressure (P), Shear (S) and Rayleigh (R) waves.

in material science and other engineering disciplines, where destructive and non-destructive testing results can be processed to recover values for the material parameters, including geometric characteristics [3]. Essentially, researchers are faced with inverse problems of mechanics, whereby available data must be utilized to extract as much information as possible for the structure or system in question [4].

In this work, special emphasis is given to Green's function for a 3D continuum as the analytical solution for representing the elastic wave fields that develop due to a buried source, see Fig. 2. A recent solution using potentials was recently developed by the authors [5] and comprise two parts, one representing the full space and the second part acting as a correction to the first part in the case a horizontal free-surface exists. Viewed otherwise, the first part is the homogeneous solution to a system of three coupled, second order partial differential equations, while the second part is a

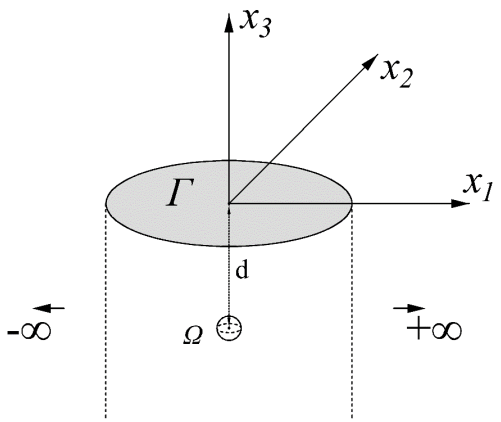

Fig. 2. Viscoelastic semi-infinite continuum with free surface Γ and volume Ω under waves emanating from a cavity approximating a point source in the limit as the cavity radius tends to zero.

particular solution that satisfies the boundary conditions of a traction-free surface. It should be noted that such solutions are difficult to come by and in fact machine learning (ML) techniques have been used to reproduce them. In here, ML will be used for a different purpose, namely to solve inverse problems in elastodynamics.

Machine Learning and Green's Functions. From a mathematical viewpoint, the numerical solution of partial differential equations (PDE) is one of the most computationally intensive challenges in mathematical physics, but has wide applicability in engineering science and technology. As a result, new methods of solution are sought, with ML playing a prominent role. More specifically, what is labelled as 'deep learning' neural networks are being developed over the last few years [6–8] to overcome the difficulty that methods such as finite elements have in representing complex functions with basis functions defined at the element level. The deep learning NN operate as a 'black box' providing a first try at solving PDE's. As usual, the NN parameters are determined through minimizing a functional comprising a part involving the dependent variable(s) so that it fits the boundary conditions and a part involving the forcing function term that minimizes error in the collocation points. More information on the implementation of deep learning in a Python environment can be found in [9], while recently Ref. [10] provided a benchmark suite based on physics-informed neural operators for the Burger's equation as a means to evaluate NN developed by other researchers.

Although in principle ML can be used to approximate any function with high accuracy, in practice evaluating complicated functions remains challenging and requires much computational effort [11]. Also, ML have been proposed as an alternative to

numerical methods such as finite elements [12]. Given that there is no unified method for evaluating the various categories of Green's functions, which are an essential component in the development of boundary integral equation methods, a recent publication [13] reported a NN approach for the numerical approximation of a pulsating Green's function in hydrodynamics, a problem involving the free surface of the fluid. Their method used optimization algorithms for gradient descent, and the calculation domain was subdivided into a number of zones. Another development of a Green's function in the frequency domain using ML is reported in [14], where the NN output is the scattered Green's function for a particular source location. Using the homogeneous background Green's function analytical solution, this NN is trained by the output Green's function and its spatial derivatives to the wave equation expressed in terms of the perturbed Green's function. In another recent application [15], the equations of 2D elasticity in solid mechanics under various boundary conditions were numerically solved by an ensemble of physics-informed NN. Finally, given that Green's functions are not available for non-linear boundary value problems (BVP) because the principle of superposition no longer holds, a flexible deep-learning approach to solve such problems using a dual-encoder approach was proposed [16]. The encoder discovers an invertible coordinate transformation that linearizes the nonlinear BVP and identifies both a linear operator and a Green; function that can be used to solve the original problem. Applications include the nonlinear Helmholtz and Sturm-Liouville problems, as well as the 2D nonlinear Poisson's equation.

Data Analysis and Monitoring. Data analysis can be performed in either of two ways, by (i) physics-based modeling, where the experimentally-obtained response data is coupled with analytical-numerical models or by (ii) data-driven modeling where the statistical correlation between the various response data sets is investigated without accounting for the physics of the structural behavior [17]. More specifically, physics-based models usually provide information in the form of numerical models with updated parameters, such as material properties, boundary conditions, and connectivity. On the other hand, date-driven models yield the experimentally obtained mechanical properties (e.g. experimental mode shapes in the case of structural dynamics) and base any estimates of the structural condition on an established benchmark state. Thus, the benchmark values of the experimentally obtained mechanical properties are compared to the newly extracted properties, which comprise the current state. Finally, hybrid approaches combining the two aforementioned methods ones have also been reported [18].

In terms of experimental work and field measurements, and especially for the purposes of newly developed structural health monitoring (SHM) approaches, the data-driven models have led to the development of algorithms based on mathematical models which are embedded into microcontrollers within wireless sensors that allow

for on-board data analysis [19]. The motivation behind this is to reduce wireless transmission of data, which despite its advantages has been proven power-consuming and often unreliable. Furthermore, it is possible to eliminate the need for extensive data storage systems, which is a problem when long-term SHM is carried out. Thus, wireless SHM systems have evolved into smart systems capable of autonomously analyzing structural response data on board and a recent application can be found in [20].

2 Mathematical Formulation

The viscoelastic material is described by the Zener constitutive equation with fractional derivatives [5] of order α in the frequency domain:

$$(1+p(i\omega)^{\alpha})\,\sigma_{ij}(\boldsymbol{x},\omega)=C_{ijkl}\,(1+q\,(i\omega)^{\alpha})\,\varepsilon_{kl}(\boldsymbol{x},\omega)\ . \tag{1}$$

The model coefficients are $p\geq 0$, $q\geq 0$ and $\alpha\in[0,1]$. Next,

$$\lambda C_{ijkl}=\delta_{jk}\delta_{pq}+\mu\,(\delta_{jp}\delta_{kq}+\delta_{jq}\delta_{kp}) \tag{2}$$

is the elastic, isotropic stiffness tensor, $\lambda\mu>0$ are the Lame constants and σ_{ij}, ε_{kl} are the stress and strain tensors. Also, all indices vary as $ijkl=123$ and ω is the frequency.

Under the assumption of small deformations, the strain-displacement relation is

$$\varepsilon_{kl}(\boldsymbol{x},\omega)=\left(u_{k,l}(\boldsymbol{x},\omega)+u_{l,k}(\boldsymbol{x},\omega)\right)/2\,, \tag{3}$$

where commas denote partial differentiation with respect to the spatial coordinates and the summation convention over repeated indices is implied. The dynamic equilibrium equations in the frequency domain for the viscoelastic continuum, written in terms of the displacements u_i, are

$$\sigma_{ij,j}(\boldsymbol{x},\omega)+\rho\tilde{\omega}^2u_i(\boldsymbol{x},\omega)+\gamma F_{0i}(\boldsymbol{X}_0,\omega)=0\,, \tag{4}$$

where ρ is the material density and $\tilde{\omega}=\sqrt{1+p\,(i\omega)^{\alpha}/1+q\,(i\omega)^{\alpha}}\omega$ is the damped frequency. Also, $\gamma=1/0$ is a conditional multiplier when considering / ignoring an embedded dynamic point source at $\boldsymbol{X}_0$, given as $F_i(\boldsymbol{x},\boldsymbol{X}_0)=\delta(\boldsymbol{x}-\boldsymbol{X}_0)\,\delta_{ij}F_{0j}$. We have that $F_{0i}=(F_{01},F_{02},F_{03})$ are amplitudes, δ_{ij} is the Kronecker symbol and δ is the Dirac delta function.

3 Green's Functions for the Viscoelastic Halfspace

The topic of Green's functions was recently reviewed by the authors [5]. As shown in Fig. 2, we seek a solution of a boundary-value problem (BVP) that will yield

the frequency-dependent, 3D displacement Green's function $G^*_{ij}(\boldsymbol{x}, \boldsymbol{\xi}, \omega)$ at receiver point $\boldsymbol{x}$ due to a point impulse at source point $\boldsymbol{\xi}$ in the three principal directions and in the presence of a traction-free horizontal plane, i.e., for the isotropic, homogeneous viscoelastic half-space. Similarly,

$$T^*_{ij}(\boldsymbol{x}, \boldsymbol{\xi}, \omega) = C_{ijkl} G^*_{km,l}(\boldsymbol{x}, \boldsymbol{\xi}, \omega)\, n_m\,, \tag{5}$$

is the corresponding traction Green's function, with n_m the outward normal at $\boldsymbol{x}$. The boundary conditions that must be satisfied are the radiation (Sommerfeld) condition at infinity and the traction-free surface $t_j = \sigma_{ij} n_j = 0$.

The Green's function G^*_{ij} solves the following partial differential equation:

$$\sigma_{ijm,i}(x, \xi, \omega) + \rho \tilde{\omega}^2 G^*_{jm}(x, \xi, \omega) = -\delta_{jm} \delta(x - \xi)\,, \quad x, \xi \in R^3_- \tag{6}$$

that satisfies the boundary condition along $x_3 = 0$, i.e., the horizontal free surface Γ_f

$$T^*_{jm}(\boldsymbol{x}, \boldsymbol{\xi}, \omega) = \sigma_{ijm} n_i = C_{ijkl} G^*_{km,l}(\boldsymbol{x}, \boldsymbol{\xi}, \omega)\, n_i = 0\,. \tag{7}$$

The Green's function can be decomposed into two parts as

$$G^*_{ij}(x, \xi, \omega) = U^*_{ij}(x, \xi, \omega) + W^*_{ij}(x, \xi, \omega)\,, \tag{8}$$

where U^*_{ij} is a fundamental solution under radiation boundary conditions and W^*_{ij} is a smooth function which solves the homogeneous part such that the complete solution G^*_{ij} satisfies the boundary condition.

The basic building block in the solution for both components of the Green's function is the displacement potential defined as $\varphi_{\mathrm{P}}(r\omega) = \exp(k_{\mathrm{P}} r)/r$ for P-waves and $\varphi_{\mathrm{S}}(r\omega) = \exp(k_{\mathrm{S}} r)/r$ for shear waves, where $k_{\mathrm{P}}, k_{\mathrm{S}}$ are the corresponding wave numbers and r is the radial distance between source point ξ and receiver point $\boldsymbol{x}$. This solution was developed by the authors [5] and numerical implementation details will be reported in a later publication.

4 Computational Model

See Fig. 3 for the computational grid used to model one-quadrant of the material from the free surface to the depth of placement of the unit impulse source. Note that nodes 01, 10, 90 are the location of the receivers for which plots will be shown in what follows. The material properties and information relevant to the description of the half space are given in Table 1.

At each node shown in Fig. 3, displacement components $U_x = U_1$, $U_y = U_2$, $U_z = U_3$ are computed as functions of frequency and subsequently transformed (by inverse FFT) to the time domain.

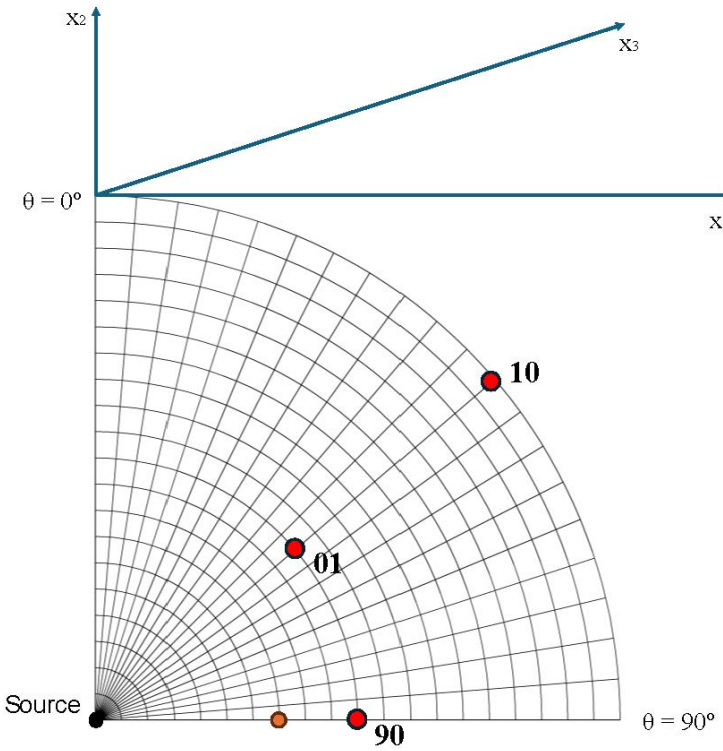

Fig. 3. 400-node grid of a fixed source-multiple receiver configuration at the upper left quadrant on the X-Z plane of the 3D viscoelastic continuum.

Table 1. Viscoelastic continuum material properties

Wave speeds $c_{\mathrm{P}} = 320$ m/s and $c_{\mathrm{S}} = 185$ m/s	Poisson's ratio $\nu = 0.25$
Material density $\rho = 2.1$	Viscoelastic coefficient $\eta = 0.5\%$
Source at depth $d = -40$ m and receivers	Wave speeds $c_{\mathrm{P}} = 320$ m/s & $c_{\mathrm{S}} = 185$ m/s
placed along a 40 m radius sweeping from	Point type of source:
$\theta = 0^\circ$ (vertical) to $\theta = 90^\circ$ (horizontal)	Unit impulse in the time domain

Lissajou plots: These resemble phase diagrams and key parameters are the frequency ratio (value of 1.0 implies the same frequency) and the phase difference (ranging from 0 to π) between the dependent variables. These are shown in Figs. 4–6 for the three nodes marked in the mesh of Fig. 3. However, these plots do not seem to give enough variation for a given displacement component to differentiate between a full space and a half space signal.

Spectogram plots: These are subsequently constructed from the 2 sec duration

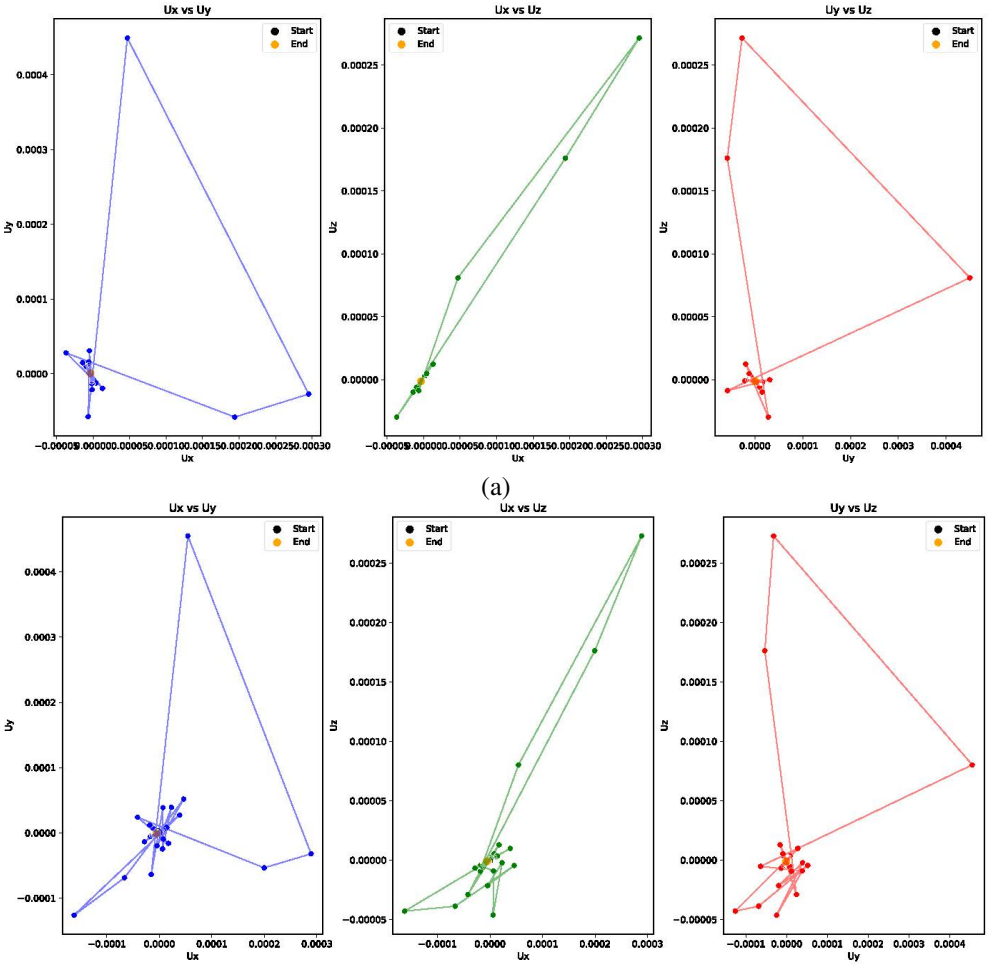

(a)

(b)

Fig. 4. Lissajou plots for the U_x, U_y, U_z displacement components at node 01 in the (a) full space and (b) half space.

U_x, U_y, U_z displacement records, using a 32 Hz sampling ratio, a 16-point Hanning window with a 15-point overlap, see Fig. 7 for the full space and Fig. 8 for the half space.

By comparing both categories of spectograms, we observe that for the first 1 sec of the displacement response (*see arrow no. 1*) of the continuum to the unit impulse source, we have a signal comprising the entire frequency band of the problem. This band is specified selecting by the time step, and the number of time points comprising

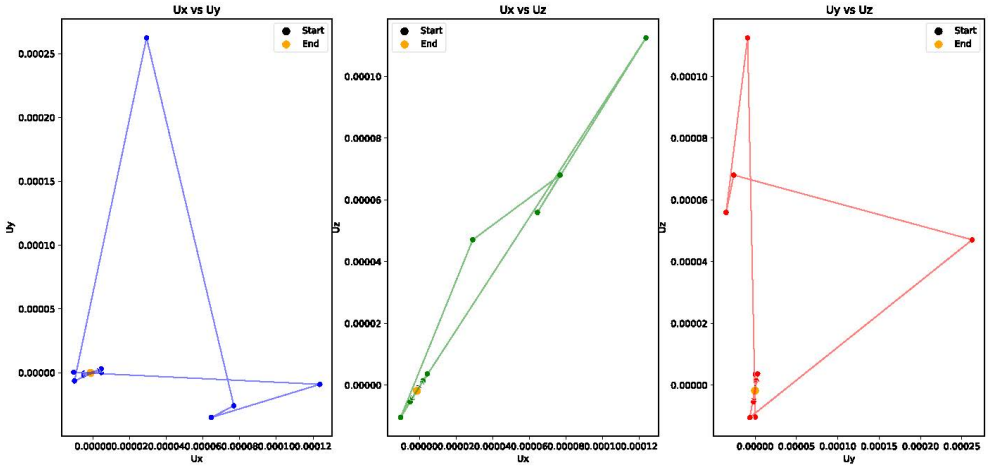

(a)

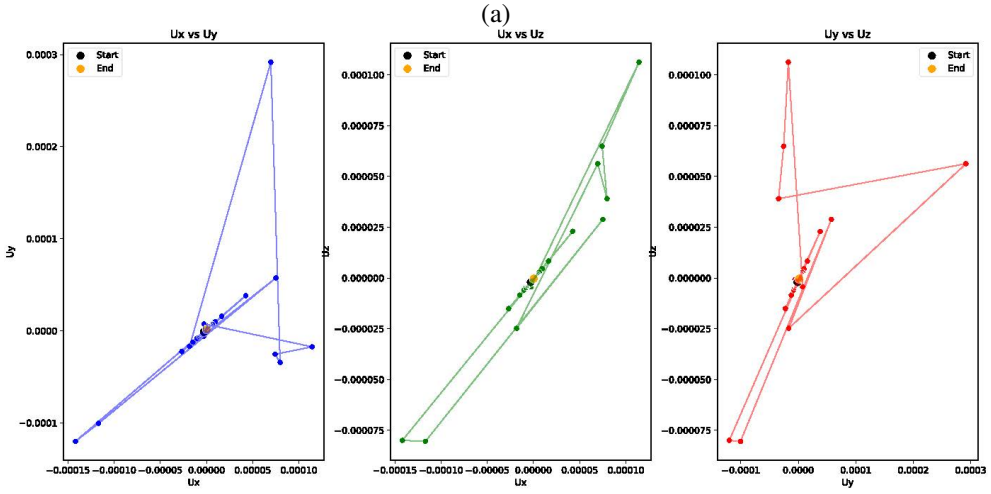

(b)

Fig. 5. Lissajou plots for the U_x, U_y, U_z displacement components at node 10 in the (a) full space and (b) half space.

the total time of interest. In the case of the halfspace, the reflection of the elastic waves from the horizontal free surface returns as a second signal to the receiver and also contains the same frequency band (*see arrow no. 2*). Finally, the frequency resolution of the pictures furnished by the spectograms can be enhanced if the time step in the numerical evaluation of the Green's function is reduced.

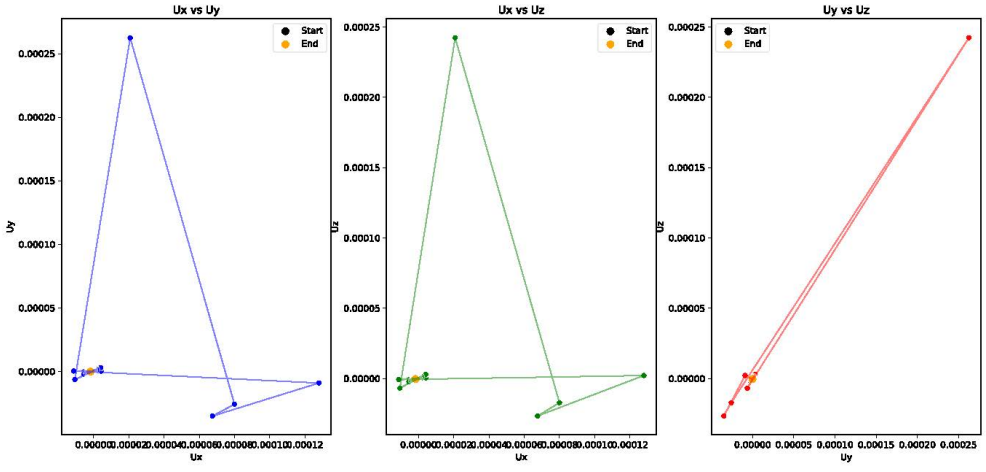

(a)

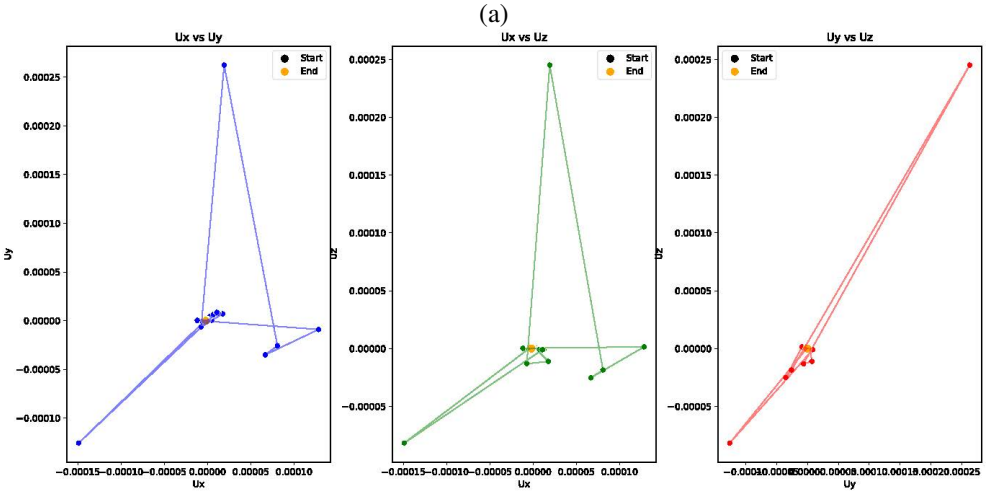

(b)

Fig. 6. Lissajou plots for the U_x, U_y, U_z displacement components at node 90 in the (a) full space and (b) half space.

5 CNN Development

This type of CNN development was recently presented by the authors [20]. The CNN operates as *input – filter – output* with $16 \times 9 \times 9 \times 3 = 3688$ starting points, see Fig. 9. This is followed by minimization of a cost function with respect to all these points. Simply stated, the output is recognition of an input signal by the CNN as corresponding to either a full or to a half space.

CNN Building Details: The spectograms are essentially images that are used as

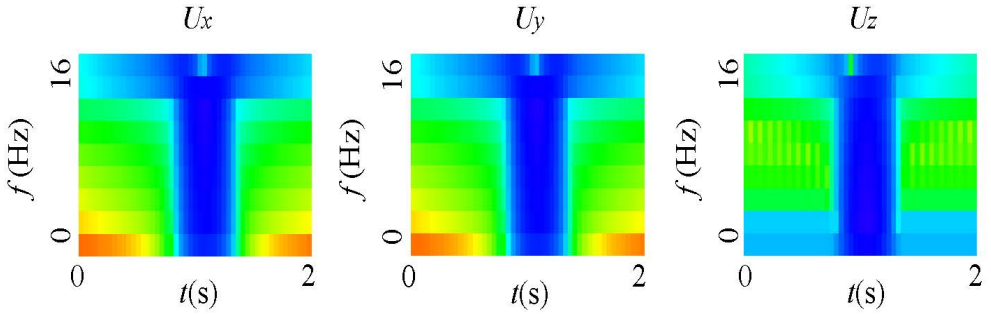

Fig. 7. Spectograms for the full-space: The receıver is placed at the orange color area: Blue-strong; Green-weak.

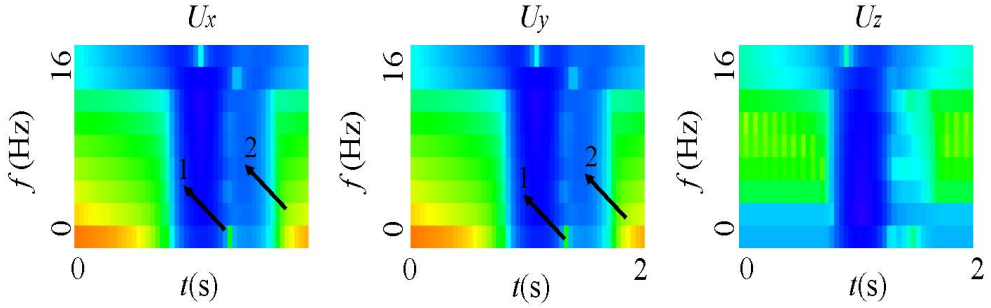

Fig. 8. Spectograms for the half-space: The receiver is placed at the orange color area area: Blue-strong; Green-weak.

input for a given CNN development. For each of the 400 nodes, we produce 3 spectograms corresponding to the three displacement components $U_xU_yU_z$. Thus, the CNN comprises 3 entries, each receiving an image of pixel size $180 \times 180 \times 3$. The convolution comprises 16 kernels of size 9×9 and yields 16 features maps of size 172×172. To each map, the operator *max_pooling* of size 8×8 is applied, thus preserving the largest number present in each sub-area of the 16 tables. This procedure is applied to each of the 3 entries, which are concatenated in 48 tables of size 21×21.

The tables are converted into a uni-dimensional array using the command *flatten* with element size 21168. This is followed by a plane of 1024 neurons and a final level *softmax* that converts numerical values into probabilities. The CNN develped here uses the algorithm *adam* for training purposes with a learning parameter equal 0.001. The smaller the learning parameter is, the slower the learning process, but the better the chances of the CNN spotting small parameter values. The cost function minimized by the *adam* algorithm is the *SparseCategoricalCrossentropy*.

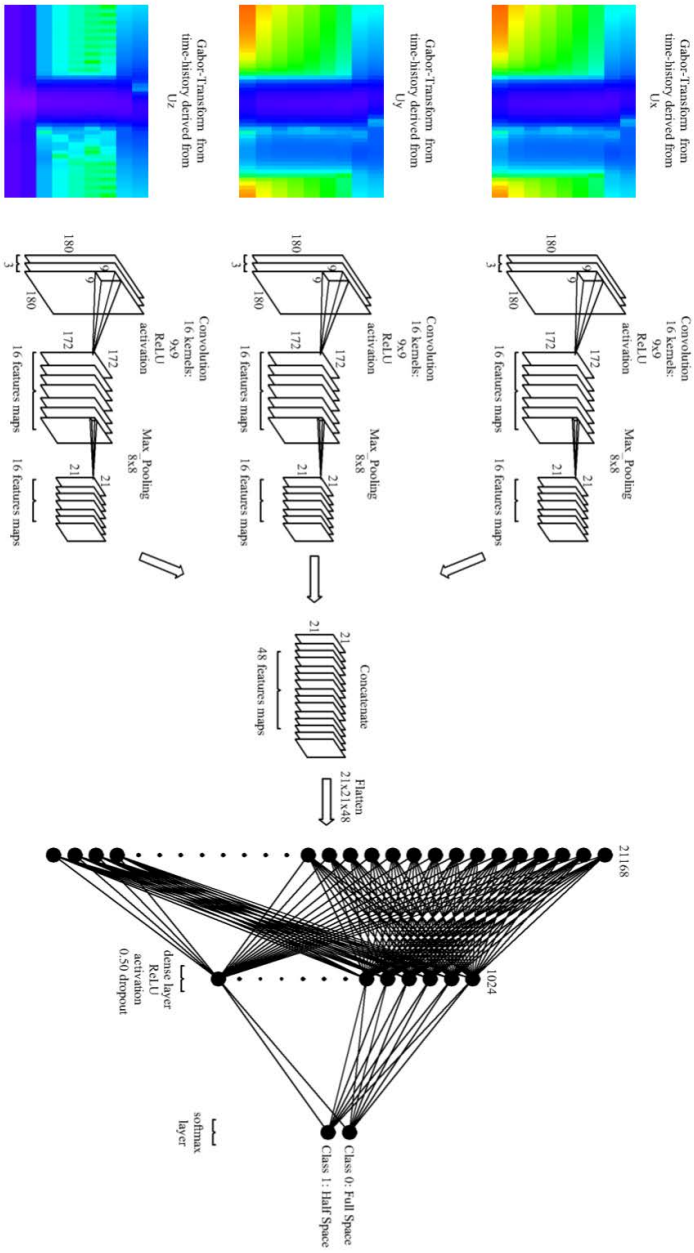

Fig. 9. CNN architecture for a 3-point input.

CNN Strategy: From a total of 800 records, 60% were used for training (480 records) and the remaing 40% for validation (320 records). The 480 records (or scenarios) were further divided into 6 batches of 80 scenarios each. CNN traing took 5 epochs, which implies that the CNN addressed all 6 batches. The corresponding loss function is plotted in Fig. 10 as a function of the *epochs*.

CNN Final Results: These are given in the form of a confusion matrix in Fig. 11, which was built by having the CNN examine all 320 validation records. Given the control circumstances under which all records were produced (namely by numerically evaluating the Green's functions for both full- and half-space), and the fact that the region where the displacements were computed was heavily influenced by the free surface, CNN identification was without error.

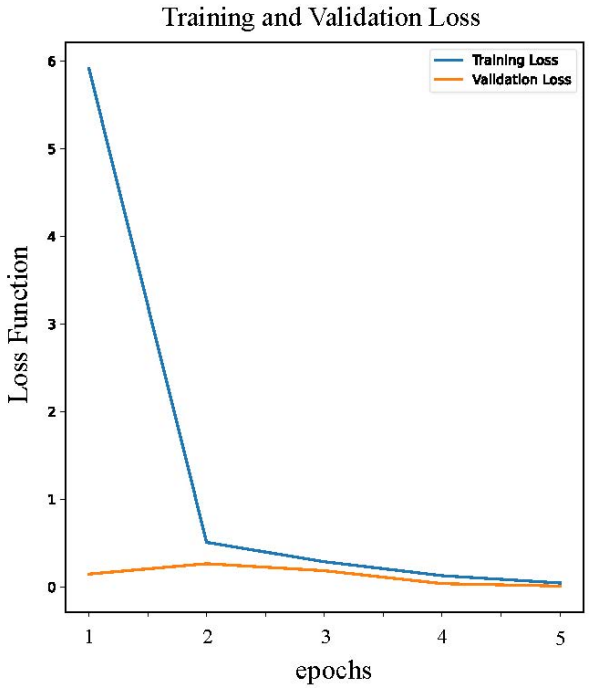

Fig. 10. Loss function attesting to error minimization in the training process: Drop with the passage of the epochs.

6 Concluding Remarks

The success of the CNN in distinguishing between the impulse-generated signals that develop in the viscoelastic continuum's vicinity to its free surface versus the

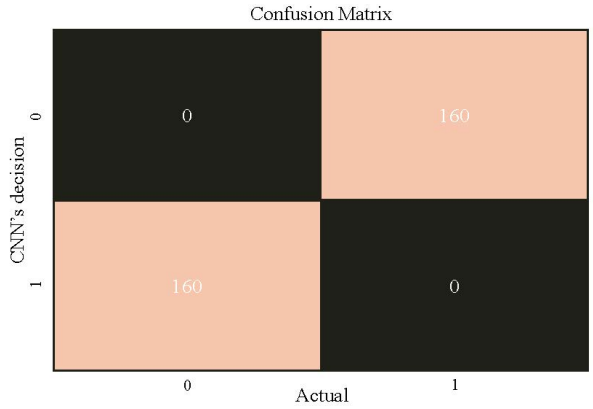

Fig. 11. Confusion matrix based on the CNN that correctly classified 320 scenarios into either the full-space (0) or the half-space (1) categories.

case where such a surface is absence is due primarily to the fact that these signals are quite different, since there is a complex pattern of wave scattering in the former case that leads to amplification effects. Furthermore, these signals are computed with high accuracy, which allows even minor differences to be detectable. Of course, this accuracy in the predictions is another proposition when training a CNN using numerically generated results and then performing the validation with actual measurements. Therefore, one future extension of this work is to conduct secure experimentally-obtained data for benchmark cases appearing in the literature so as to test the CNN under operational conditions. The final aim of the ML procedure developed in this work is to be able to estimate the depth of the source from the horizontal free surface from signals recorded in a half space, as this development finds applications, besides geophysics, in material science as well.

ACKNOWLEDGEMENT

This work is partially supported by the Bulgarian National Science Fund, contract No КП-06-H57/3/15.11.2021. The second author (G.I.D.) acknowledges the Hellenic Foundation for Research and Innovation (HFRI) for *Fellowship No. 6522* under the third call for Ph.D. fellowships.

REFERENCES

[1] W. LOWRIE, A. FICHTNER (2020) "Fundamentals of Geophysics". Cambridge University Press, Cambridge, UK.

[2] I.-K. FONTARA, S. PARVANOVA, P. DINEVA, F. WUTTKE (2015) Wave propagation due to an embedded seismic source in a graded half-plane with free-surface and sub-

surface. Part I: mechanical model and computational technique. *Journal of Theoretical and Applied Mechanics* **45**(1) 87-98.

[3] R. Brinnker, C. Ventura (2015) "Introduction to Operational Modal Analysis". Wiley, Hoboken, New Jersey, USA.

[4] D. Lesnic (2021) "Inverse Problems with Applications in Science and Engineering". CRC Press, Boca Raton, Florida, USA.

[5] T.V. Rangelov, P.S. Dineva, G.D. Manolis (2023) A Dynamic Green's function for the Homogeneous Viscoelastic and Isotropic Half-Space. In: A. Slavova (eds) "New Trends in the Applications of Differential Equations in Sciences". NTADES 2023. Springer Proceedings in Mathematics & Statistics, vol. 449, pp. 151-160. Springer, Cham. Also appears in arXiv.2308.08184v2

[6] K. Xu, B. Shi, S. Yin (2018) Deep learning for partial differential equations. Paper CS230, *Deep Learning*, Stanford University, Stanford, California, USA.

[7] M. Raissi, P. Perdikaris, G.E. Karniadakis (2019) Physics-informed neural networks: A deep learning framework for solving forward and inverse problems involving nonlinear partial differential equations. *Journal of Computational Physics* **378** 686-707.

[8] E. Lagaris, A. Likas, D.I. Fotiadis (1998) Artificial neural networks for solving ordinary and partial differential equations. *IEEE Transactions on Neural Networks* **9** 987-1000.

[9] F. Chollet (2021) "Deep Learning with Python". Manning Publications Company, Shelter Island, New York, USA.

[10] S.G. Rosofsky, H.A. Majed, E.A. Huerta (2023) Applications of physics informed neural operators. *Machine Learning in Science and Technology* **4** 025022.

[11] G.E. Karniadakis, I.G. Kevrekidis, L. Lu, P. Perdikaris, S. Wang, L. Yang (2021) Physics-informed machine learning. *Nature Review Physics* **3** 422-440.

[12] S. Rezaei, A. Harandi, A. Moeineddin, B.X. Hu, S. Reese (2021) A mixed formulation for physics-informed neural networks as a potential solver for engineering problems in heterogeneous domains: Comparison with finite element method. *Computer Methods in Applied Mechanics and Engineering* **401**(B) 115616.

[13] S. Huang, R. Zhu, H. Chang, H. Wang, Y. Yu (2021) Machine Learning to approximate free-surface Green's function and its application in wave–body interaction. *Engineering Analysis with Boundary Elements* **134** 35-48.

[14] T. Alkalifah, C. Song, U. Bin Wahid (2020) Machine Learning Green's functions that approximately satisfy the wave equation. *Society of Exploratory Geophysicists International Exposition and 90th Annual Meeting*. Houston, USA, pp. 2638-2642.

[15] A.D. Mouratidou, G.A. Drosopoulos, G.E. Stavroulakis (2024) Ensemble of physics-informed neural networks for solving plane elasticity problems with examples. *Acta Mechanica* **234** 6703-6722.

[16] C.R. Gin, D.E. Shea, S.L. Brunton, N. Kutz (2021) Deep Green: Deep learning of Green's functions for nonlinear boundary-value problems. *Scientific Reports* **11** 21614.

[17] M. AZIMI, A.D. ESLAMLOU, G. PEKCAN (2020) Data-driven structural health monitoring and damage detection through deep learning: State-of-the-art review. *Sensors* **20**(10) 2778.

[18] A. ENTEZAMI, H. SARMADI, B.S. RAZAVI (2020) An innovative hybrid strategy for structural health monitoring by modal flexibility and clustering methods. *Journal of Civil Structural Health Monitoring* **10** 845-859.

[19] M. ABDULKAREM, K. SAMSUDIN, F.Z. ROKHANI, M.F.A. RASID (2019) Wireless sensor network for structural health monitoring: A contemporary review of technologies, challenges, and future direction. *Structural Health Monitoring* **19**(3) 693-735.

[20] G.I. DADOULIS, G.D. MANOLIS, T. ZURIQAT, K. DRAGOS, K. SMARSLY (2024) Towards detecting damage in lightweight bridges with travelling masses using Machine Learning. *European Conference on Computing and Construction (EC3)*, Chania, Crete, Greece, 14-17 July 2024.